Full Length Article

Digging into the friction reduction mechanism of organic friction modifiers on steel surfaces: Chains packing vs. molecule–metal interactions

Nicolò S. Villa [a], Lucia Bonoldi [b], Giulio Assanelli [b], Marcello Notari [b], Andrea Lucotti [a], Matteo Tommasini [a,*], Herma M. Cuppen [c], Daria R. Galimberti [c,*]

[a] Dipartimento di Chimica, Materiali e Ingegneria Chimica "G. Natta", Politecnico di Milano, Piazza Leonardo da Vinci 32, 20133, Milano, Italy
[b] Eni SpA, Research & Technological Innovation, Downstream R& D Centre, Via Felice Maritano 26, 90027, San Donato Milanese, Milano, Italy
[c] Institute for Molecules and Materials, Radboud University, Heyendaalseweg 135, 6525 AJ, Nijmegen, The Netherlands

ARTICLE INFO

ABSTRACT

We present a study of five commercially available Organic Friction Modifiers (OFMs) that combines micro-Infrared reflection absorption spectroscopy (IRRAS), classical MD, and DFT/DFT-MD computational methods. We investigate the relation between the molecular structure of the OFMs and their temperature-dependent friction performance. Classical dynamics simulations show that at low temperatures, the OFM molecules, arranged in self-assembled monolayers, undergo collective torsional motion during a friction event. This becomes progressively easier as temperature increases, resulting in lower friction coefficients, until a temperature where these collective motions cannot be maintained anymore, leading to an increase of the friction coefficient. Static DFT calculations indicate that the strength of the packing between OFM molecules determines the friction performance. The temperature at which the collective behavior fails coincides with the temperature at which the packing-free energy is found to diminish.

1. Introduction

Friction modifiers are lubricant additives that have an essential role in modern industry, as friction between metal – and in particular steel surfaces – is one of the main causes of energy waste worldwide, from industrial processes to common household appliances. It is estimated that roughly 23% of the global energy consumption is wasted on overcoming tribological phenomena [1,2]. Saving this energy would be beneficial from both an economic and an environmental perspective. Friction modifiers are added in complex lubricant blends for the purpose of reducing friction between two sliding surfaces [3]. In recent years, the toxicity and the negative environmental footprint of the traditional steel friction modifiers, e.g., molybdenum dithiocarbamates (MoDTCs) and zinc dithiophosphates (ZnDTPs), triggered the development of alternative, greener, lubricant formulations that can maintain efficient friction reduction while taking a lower toll on the environment. While ZnDTPs remain irreplaceable additives because of their anti-wear properties, Organic Friction Modifiers (OFMs) are regarded as the best candidates as friction-reducing additives due to their low-SAPS (Sulphated Ash, Phosphorus, and Sulfur) content and ease of manufacture [4]. OFMs are amphiphilic molecules composed of an apolar tail (usually an alkyl chain) and a polar head containing C, N, and O atoms. The function of the headgroup is to guarantee stable adsorption

on the steel surfaces of common automotive engine parts. OFMs adsorb on the steel surface forming well-organized Self-Assembled Monolayers (SAMs) that act as a separating layer between the surfaces and the main bulk of the lubricant [2,5]. A wide array of experimental techniques [4–16] have been applied to link the friction behavior of OFMs at different working conditions (temperature, pressure, sliding speed) to molecular structure information. However, due to the complexity of the phenomena involved, experimental techniques alone cannot solve the riddle and they need to be augmented with computational methodologies. Computational techniques such as tight-binding calculations [4], Density Functional Theory (DFT) [12,17], Molecular Dynamics classical simulations (MD) [18–26], and Non-Equilibrium Molecular Dynamics (NEMD) [27,28] have been used to gain insights on the adsorption properties and friction behavior of OFMs. Nevertheless, it is still unclear which characteristics of the molecular structure of the OFMs determine the friction-reducing properties at different temperatures, despite all computational efforts. This missing information seriously hinders the rational development of new, more efficient, and greener OFMs. Here we propose an interdisciplinary study combining experimental tribological data, experimental IRRAS spectroscopy, static DFT calculations, DFT-MD simulations, and classical MD simulations to elucidate the
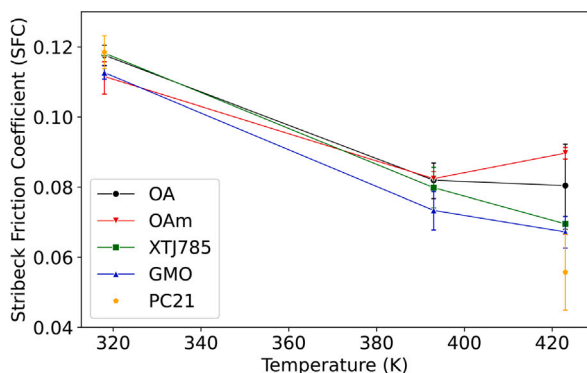

Fig. 1. Measured Stribeck Friction Coefficient (SCF) of OFMs plotted with respect to temperature. Due to the reduced number of data points for PC21 at 393 K, we did not include this data in the plot.

behavior of five OFMs adsorbed on the α-Fe$_2$O$_3$(0001) as a function of temperature. The insights provided by this study help us understand the role of the packing interactions between the OFM molecules in the SAM that control their friction performances and can provide crucial information for the molecular design of improved OFM additives.

2. Results & discussion

2.1. Experimental friction coefficients

To compare different temperatures and OFMs more easily, instead of using the full Stribeck curves [29–32], we choose to use the Stribeck Friction Coefficient (SFC) [33]. The Stribeck Friction Coefficient (SFC) is the area under the Stribeck curve and is proportional to the energy loss due to friction if η/P is constant, where η is the viscosity and P the normal load. In our experiments, the curves were obtained maintaining a constant normal load of 30 N and 50% sliding/rolling ratio. The SFCs reported here are obtained by integrating the friction curve between 0.004 m/s and 2 m/s on the logarithmic scale to prevent that the SFC is dominated by the mixed regime. This corresponds to integrating the boundary and mixed regimes only. In the boundary lubrication regime, the tribofilm is very thin (order of nanometers), and we expect the OFM to dominate the shape of the Stribeck curve [34]. The boundary-mixed regimes SFC was measured at three temperatures: 45, 120, and 150 °C (318, 393, and 423 K), which are in the range of working temperatures found in common automotive engines. Fig. 1 plots the SFCs of the investigated OFMs at the three different temperatures (See Section 4.2.1, for more details on the measurements). All OFMs show a significant reduction of the friction coefficient between 318 K and 393 K. The coefficients at 423 K indicate a lowering in the slope or even an increase in the fiction coefficient again. The latter means that there is a minimum in the friction coefficient within the probed temperature regime. OAm will only be an effective friction modifier at temperatures below this minimum. Notice that for OA, around 423 K, the measured data start to show strong fluctuations in the performance, indicating that we are reaching the limit of the working region conditions also for this OFM.

The behavior of the friction coefficient with the temperature (decrease → plateau → instability/increase) appears general for all the OFMs from a qualitative point of view. The molecular structure however determines the exact critical temperature for deterioration of the OFM performance and imposes strict conditions on the temperature window where each OFM is effective. To design an OFM with the ideal temperature window, it is hence important to *(i)* understand the mechanism behind the deterioration behavior and *(ii)* determine the molecular properties that set the critical temperature. To answer the first point, we simulated the action of a piston, on a model OFM

tribofilm by classical atomistic MD simulation, to gain an atomistic insight (See Section 4.3.3 for more details). To answer the second point, we performed DFT simulations of the adsorbed configurations of the OFMs on the surface of α-Fe$_2$O$_3$(0001) (see Section 4.3.2), and evaluated their adsorption energies, separating the contributions of the interaction of the OFM with the surface, and the packing interactions between the OFM molecules in the SAM. Considering the experimental conditions in which the SAM of OFMs is prepared, we expect to be in the high coverage regime. Therefore, a surface density of one molecule per unit cell was chosen for both the classical molecular dynamics and DFT simulations. Once the surface is relaxed after the adsorption of the molecules, this corresponds to a coverage of 4.5 nm^{-2} at the 0 K-optimized DFT level and of 4.2 nm^{-2} at the NpT molecular dynamics classical force field level (see Tables S1 and S2 of the Supporting Information for more details).

2.2. Behavior of the tribolayer with temperature

For our MD simulations, we chose to reduce the number of carbons in the alkyl chain of OA to 6 carbon atoms (For the discussion of the reasons for this choice see Section 4.3.1). Our model system then consists of OA$_{C6}$ adsorbed in a bidentate bridging configuration on two α-Fe$_2$O$_3$(0001) slabs facing each other. The space between the two slabs is filled with molecules of squalane to simulate the base lubricant oil. The choice of the bidentate bridging adsorption geometry has been suggested by our DFT data which show that after the adsorption, a proton from the headgroup of the OFM transfers to the surface (Fig. 2), with the exception of OAm$_{C6}$ in the monodentate configuration and XTJ785$_{C6}$. The impact of the piston was simulated by applying a velocity of ± 0.5 m/s to the hematite slabs in opposite directions, yielding a total relative velocity of 1 m/s. To investigate the effect of temperature, simulations were carried out at 300, 420, and 500 K. The simulations were run for a total of 2.5 ns, and the sliding direction was inverted two times: at $t = 0.5$ ns, and at $t = 1.5$ ns.

Three order parameters – O, θ, and d – are monitored during the simulations, to have a more quantitative understanding of the molecular changes. The parameter O is a measure of the amount of disorder in the positioning of the headgroups at the surface (i.e. the presence of disordered domains). It is defined as the scalar product between the vector $\vec{v}_i$ connecting the two terminal oxygens of one molecule's headgroup and a similar vector $\vec{v}_j$ for a nearest neighbor molecule in the SAM

$$O = \vec{v}_i \cdot \vec{v}_j \tag{1}$$

We will typically plot this order parameter as a distribution. The dihedral θ parameter describes the orientation of the molecules within the SAM. It is defined as the dihedral angle $\theta = O_1 \widehat{C_1 C_2} C_3$ between one terminal oxygen atom of the molecule and the third carbon of the alkyl chain. After equilibration θ is distributed around two angles centered at $\theta = -90°$ and $90°$. To monitor the evolution of this parameter during the simulation, we chose to plot the percentage of molecules with $\theta > 0°$ (Fig. 4). Finally, the third parameter d is the end-to-end distance $d = |C_1 C_6|$ of the alkyl chain of the molecules. It describes the amount of torsional deformation that occurs overall on the molecules. Fig. 3a plots the distribution of O for three different temperatures before and after the sliding simulations. At both 300 K and 420 K, it shows a single peak in the distribution around $O = 1$, indicating that the heads of the model OFM are well-ordered on the surface. The snapshot given in Fig. 3b confirms that indeed the carboxylic heads are parallel to each other. Even when stress is applied, this order remains almost unchanged. The chains instead collectively react with the direction of friction during tribological sliding. As can be seen from Fig. 4, at both 300 K and 420 K the chains first gradually align for $\theta < 0°$ during the first 0.5 ns. At this point, the motion is inverted and the alignment of molecules also flips, until the motion is inverted again at the 1.5 ns mark. This is in agreement with previous studies [27]. Meanwhile, the
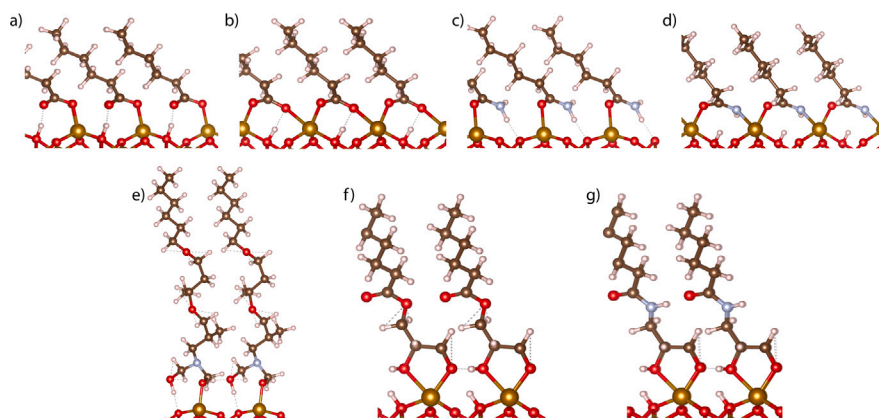
Fig. 2. Adsorption geometries after optimization of OA_{C6} in the (a) monodentate and (b) bidentate bridging configurations; OAm_{C6} in the (c) monodentate and (d) bidentate bridging configuration; (e) $XTJ785_{C6}$ in its monodentate configuration; (f) GMO_{C6} in the bidentate chelating configuration; (g) $PC21_{C6}$ in its bidentate chelating configuration. Atoms are colored red for oxygen, orange for iron, blue for nitrogen, brown for carbon, and white for hydrogen.
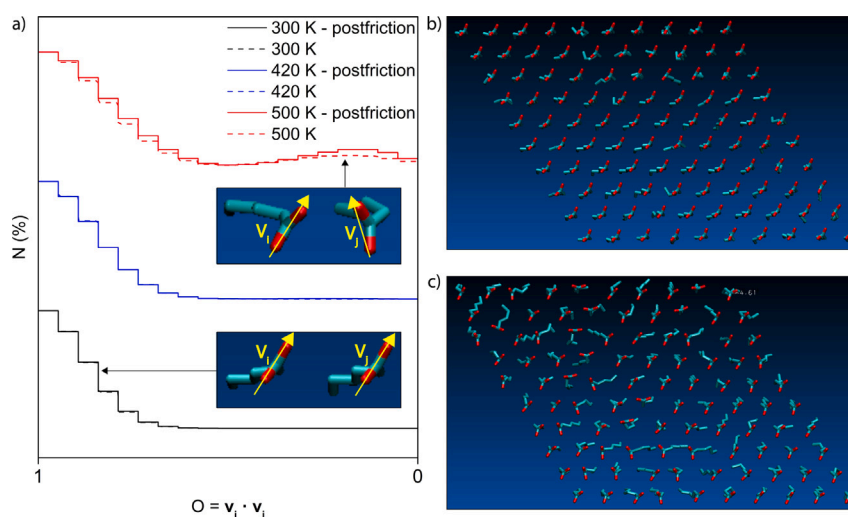

Fig. 3. (a) Distribution of the parameter $O = \vec{v}_i \cdot \vec{v}_j$ at 300 K (black), 420 K (blue), and 500 K (red). 2.5 ns MD evolution with 1 m/s relative sliding velocity (full lines), and 2 ns MD evolution, with no relative sliding velocity (dashed lines). On the right side of the panel: Snapshots (bottom view) of the 10 × 10 slab of OA_{C6} adsorbed on hematite after 2.5 ns classical MD run at (b) 420 K, and (c) 500 K. The hematite slab has been hidden from view for clarity purposes.

end-to-end distance decreases due to the formation of kinks along the chain to allow the tilt (Fig. 5). When the direction of motion is inverted, the molecules of the SAM quickly adjust. At 300 K, this effect is less pronounced and the inversion occurs at a lower rate and with some time delay effect. This is very evident when comparing the population of $\theta > 0°$ after 1.5 ns at 420 K with the same at 300 K. The end-to-end distances are also not as affected at 300 K as at 420 K.

At 500 K, the situation completely changes. Already with zero friction a new peak appears in the distribution $O = \vec{v}_i \cdot \vec{v}_j$ closer to 0. The film is fragmenting in ordered and disordered domains (Fig. 3c).

At the same time, the molecules of the SAM are less affected by the sliding direction, as the distributions of the θ angle show strong fluctuations during the constant sliding step, and hardly respond to the change in the slide direction (Fig. 4). Instead, they continuously flip between the two directions, as can be observed from the raw, unsmoothed data. The end-to-end distances at 500 K with and without the application of shear, are nearly unchanged, suggesting again the independence of the SAM on the stress when reaching this temperature (Fig. 5). With these data, we can provide a first interpretation of the behavior of the friction modifier SAM with temperature. At low temperatures, the SAM responds collectively to the applied shear stress by changing the torsional angles of the molecules according to the

direction of friction (Figs. 4 and 5, black lines). The SAM thus finds a more energetically favorable arrangement. This rearrangement is faster and more efficient with increasing temperature, as long as it remains below a critical temperature, resulting in less friction (Figs. 4 and 5, blue lines). However, when a critical temperature is reached, the polar heads of the molecules start to rotate individually (Fig. 3a, red line), disorder domains are formed (Fig. 3c), and therefore, the collective behavior is lost (Figs. 4 and 5, red lines). As a consequence, the friction coefficient increases. Notice that this occurs at a temperature much lower than the one required to detach the OFMs from the surface. This picture is coherent with previous computational and experimental studies on the effects of the surface coverage and sliding velocity on the OFMs performance on different surfaces [27,35–40], showing that promoting a well-organized and close-packed monolayer is instrumental for a substantial decrease of the friction. In particular, only when the surface coverage is high enough to form a compact solid-like monolayer and clear slip planes between the OFMs and the lubricant are set-up, the friction reduction properties of the OFMs are fully exploited.

2.3. Tilt mechanism and thermal disorder

The presence of a chain tilt mechanism has been proposed before on the basis of both computational and experimental evidences [27,41–43]
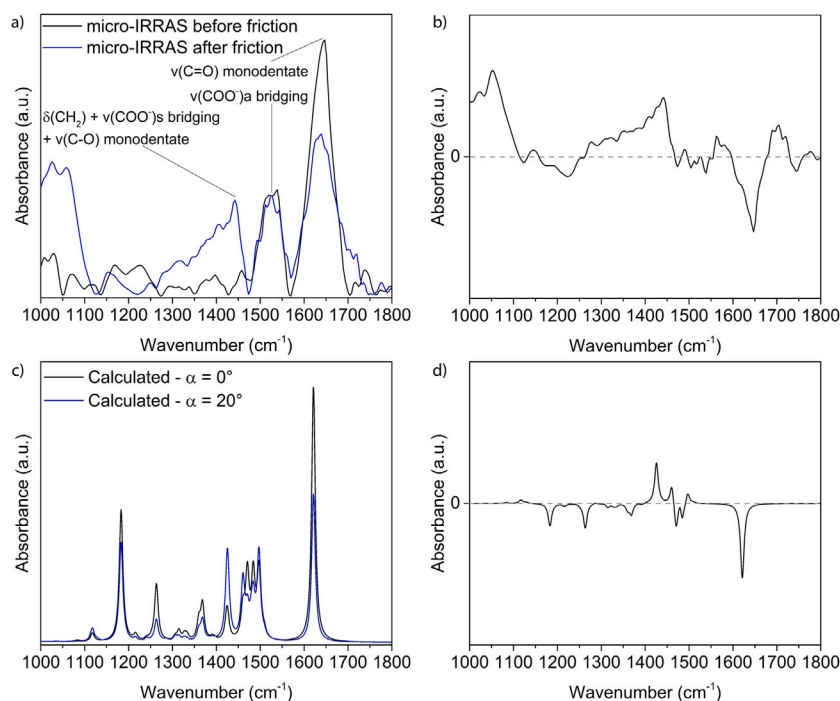
Fig. 4. Evolution in time of the dihedral angle θ of OA_{C6} at 300 K, 420 K, and 500 K after 2.5 ns MD run at 1 m/s relative sliding velocity. Inversions of motion are applied at t = 0.5 ns and t = 1.5 ns (green dashed lines).

Fig. 5. Distribution of the end-to-end distance d of the alkyl chains of OA_{C6} after 2.5 ns MD evolution at 300 K (black), 420 K (blue), and 500 K (red) (full lines). The dashed lines represent the same distribution after 2 ns evolution with no relative sliding velocity applied.

and it is confirmed here experimentally by micro-IRRAS spectroscopy. IRRAS spectroscopy is only sensitive to the IR spectral component polarized along the normal to the metal surface, i.e., only normal modes with a transition dipole moment possessing a component perpendicular to the surface are expected to appear in the spectrum. This makes IRRAS spectroscopy particularly suitable to evaluate the relative orientation of the OFM molecules with respect to the surface: if the molecule tilts compared to the surface normal, the active components change and the intensities in the IRRAS spectra are modulated. OA_{C6} is used again as a model system for all the OFMs in the discussion. The experimental micro-IRRAS spectra of OA (Fig. 6a) show very broad bands, which can be ascribed to the thermal disorder that occurs in the tribofilm already at room temperature. This is confirmed by DFT-MD simulations (see supplementary information — Section SI-4).

Still, the experimental IRRAS spectrum of OA presents clear marker bands of a structural reorganization of the SAM due to the tribological stress, as highlighted by the difference spectrum (Fig. 6b). In Ref. [12], we already proposed that the increase of the relative intensity of the δCH_2 scissoring peak at 1444 cm^{-1}, and the decrease of the IRRAS relative intensity of the C=O stretching at 1646 cm^{-1} observed in the

spectrum of the tribofilm after friction, is related to the tilt of the molecule on the surface. This was based on the analysis of the normal modes of the absorption spectra computed within the static harmonic approximation. Here we corroborate this by deconvolution of the total computed IR signal into its polarization components along specific directions to take into account the IRRAS selection rules. In a first approximation, the effect of a tilt of the molecule (chains and the polar head together) of the OFM can be modeled by computing polarized spectra at increasing tilt angles compared to the z-direction of our simulation cell (z-polarized spectra for tilts from 0 to 30 degrees are available in supplementary information — Section SI-3). Since the tilt is only accounted for mathematically, the protocol does not include the effect of the OFM head-surface interaction due to the tilt and the presence of gauche defects (clearly indicated by the end-to-end distance values obtained by the MDs, Fig. 5). Hence these spectra can only give a qualitative indication based on relative intensity changes. The change in relative intensity before and after friction observed in the experimental micro-IRRAS spectra is perfectly consistent with tilting of the SAM by 30°(Fig. 6d). A similar agreement is found for the OAm_{C6} and GMO_{C6} tribofilms, as presented in the supplementary information — Section SI-3. The spectra are calculated assuming a 1:1 monodentate:bidentate ratio. This is based on the difference in the computed electronic and free adsorption energies between the OA monodentate and bidentate configurations, which is quite small compared to kT (see Tables 3 and 6 of the S.I.).

2.4. Role of chain packing

As indicated by the previously discussed MD simulations, the friction performances of an OFM tribofilm are influenced by the presence of collective behavior of the alkyl chains. These performances are lost when surpassing a critical temperature, which suggests that the tribolayer has become unstable. Next, we study the trend in stability between the different OFMs. DFT calculations of OAm_{C6}, OA_{C6}, GMO_{C6}, $XTJ785_{C6}$, and $PC21_{C6}$ adsorbed on hematite were performed. The computed electronic adsorption energies are consistent with chemisorption, spanning between −290 kJ/mol and −465 kJ/mol. These values significantly differ from those reported by Gattinoni et al. [17], which can be attributed to the very different computational setup (i.e., functional, basis set, k-point grid, and optimization with or without lateral relaxation of the surface after the adsorption). One consequence of the different computational setups is that Gattinoni et al. were not able to find a stable OA monodentate configuration at high coverage conditions, while we found a monodentate configuration under these conditions that is almost as stable as the bidentate one. As discussed in Ref. [12], the experimental micro-IRRAS spectra show clear marker bands of monodentate configuration at 1646 cm^{-1} (C=O stretching band) and bidentate at 1524 cm^{-1} (COO$^-$ asymmetric stretching). These are indicative of the presence of both monodentate OA and bidentate in the experimental sample both before and after the friction experiment. The similar stability of the mono/bidentate configurations predicted by B3LYP agrees with the observation of clear IRRAS markers for both structures. The adsorption energy can be decomposed into two terms: the interaction of the OFM head with the surface (adhesion energy) and the interaction with adjacent molecules in the tribolayer (packing energy) (See Section 4.3.2 for the definition). The adhesion energy is dominated by the geometric placement of the head on the surface. The head-metal interactions are quite similar among the different molecules (Fig. 2) and their contribution does not follow a specific pattern with respect to the total adsorption energy (Fig. 7a). The packing energy, instead, follows almost the same trend as the adsorption energy. The interactions between adjacent OFM molecules, and consequently the shape of the SAM, can vary quite significantly among the different OFMs. OA_{C6}, OAm_{C6} and $XTJ785_{C6}$ chains interact only by dispersion interactions. In contrast, GMO_{C6} and $PC21_{C6}$ chains also interact by hydrogen bonds (Fig. 2f,g). As expected, the higher the

Fig. 6. (a) Experimental micro-IRRAS spectra of OA adsorbed on steel before (black) and after (blue) the MTM test and (b) the difference spectrum. (c) Calculated polarized spectra of all-trans OA_{C6} adsorbed on hematite, with tilt angle $\alpha = 0°$ (black) and $20°$ (blue) compared to the *z*-direction of our simulation cell (1:1 Monodentate–Bidentate ratio) and (d) the difference spectrum. The calculated frequencies presented in (c) and (d) have been uniformly scaled by a factor of 0.98 to ease the comparison with the experiments.
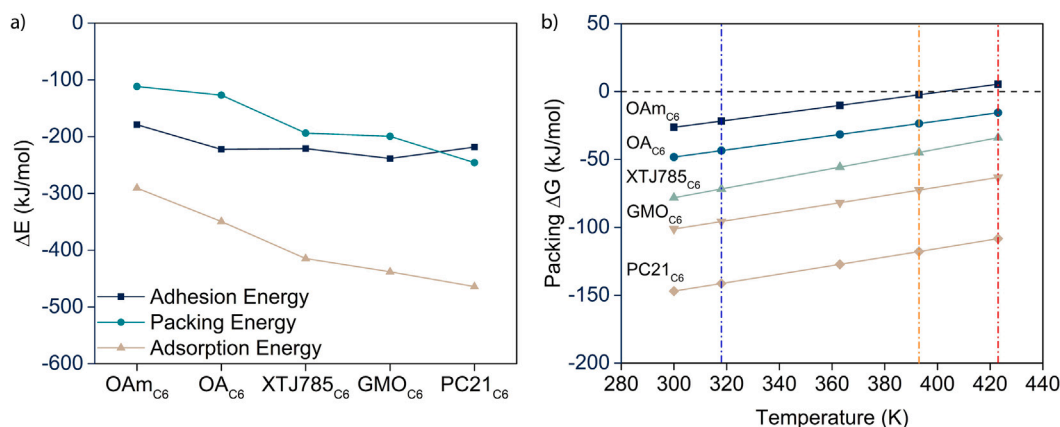
Fig. 7. (a) Plotted DFT calculated electronic adsorption, packing, and adhesion energies for each of the OFMs investigated. (b) Gibbs' free energies of packing calculated from the DFT models of the OFMs investigated.

number of hydrogen bonds, the higher the packing energy in absolute terms. Given these considerations, we expect that, if a relation between friction coefficient and adsorption energy exists, it is related to the packing energy component. However, to get at the complete picture, one has to consider the effect of temperature on the stability of the tribofilm. This can be assessed from the trend of the packing Gibbs free energies, which accounts for both the enthalpy and entropy terms (Fig. 7b). We expect packing disorder to become significant when the packing Gibbs free energy diminishes, resulting in the loss of the collective behavior of the SAM. We will refer to the temperature at which the packing Gibbs free energy reaches zero as the "packing-failure temperature". For OAm_{C6}, this occurs around 393 K, while for OA_{C6} this is above 423 K, which is consistent with the results of the MD simulations. The packing-failure temperatures of $XTJ785_{C6}$, GMO_{C6}, and $PC21_{C6}$ are all significantly higher, as the entropic component increases the relative stability of the hydrogen-bonded SAMs compared to the others. Our calculations of the free energy do not account for

anharmonicity and the presence of stress, which can shift the values for the predicted packing failure temperatures. Still, we expect the trend in packing failure temperature between the different OFMs to be accurately predicted.

Finally, we can relate our theoretical results to the experimental friction coefficient data for all OFMs investigated. To do that, we compare the calculated packing energy to friction coefficients measured at different temperatures. (Fig. 8). At lower temperatures (318 and 393 K), the friction performances of the OFMs are almost the same, independent of the strength of the packing interactions. However, this changes upon an increase in temperature. At 423 K, the friction coefficient linearly decreases with packing energy (Correlation coefficient $= -0.70$; Pearson's r = 0.0001). For the three OFMs with high packing energy, XTJ785, GMO, and PC21, the friction coefficient continues to decrease with the temperature, suggesting that the packing failure temperature has not been reached yet. However, the two OFMs with low packing energy (OAm and OA) show a stabilization or even increase of
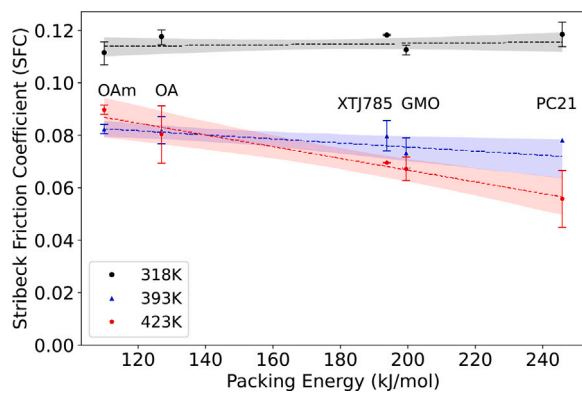
Fig. 8. Measured friction coefficient for each of the MTM samples investigated plotted with respect to the adsorption energy calculated from the DFT models. The color bands indicate the 95% confidence interval.

the friction coefficient going from 393 to 423 K, suggesting that their packing-failure temperature is either within the 393–423 K range or close to it.

Our model surfaces are idealized and lack the irregularities (roughness) of real surfaces, for instance, caused by humidity and the presence of oxygen. These features could add contributions to the effects investigated in the present paper [44,45], and it will be interesting in the future to consider these factors. Still, the experimental results can already be completely explained by the trend in packing energy. The prediction of the packing-failure temperatures from the calculations of the packing Gibbs' free energies are also in remarkable agreement. This further strengthens our confidence in the validity of the molecular mechanism that we have obtained from our combined computational approaches in explaining the friction behavior of the tribofilms at the molecular scale.

3. Conclusions

Our combined experimental and computational approach demonstrates that the tribological performances of the OFMs on α-Fe$_2$O$_3$(0001) are determined by both the adhesion interactions (interaction of the OFMs polar head with the steel surface) and the packing interactions among the apolar chains of the friction modifier. In particular, the latter determines how steeply the friction coefficient drops with temperature, as well as the critical temperature at which the friction modifier loses its friction-reducing properties. Our MD simulations show that when the tribofilms are sliding against each other the packing interactions induce a collective and coherent torsion and tilt motion of the chains. The tilt mechanism of the chains has been confirmed by micro-IRRAS spectroscopy. Recently, it has been shown [26] that the better the surface coverage and the lower the entropy losses of the OFMs during film formation, the better the tribological performance. Here we demonstrate a even more relevant role of entropy in determining the OFMs performances. The collective motion of the OFM chains is facilitated by the temperature increase, justifying the decrease of the friction coefficient. However, this works only until the enthalpy component of the free energy dominates the entropic one, thus keeping the monolayer stable. When the entropy starts to dominate, the free energy becomes positive, the monolayer becomes unstable, and an ordered packing can no longer be maintained. As a result of the formation of disordered domains of the SAM on the surface, the friction performances start worsening. When this happens, the molecules of the SAM are not moving collectively anymore, which contributes to the loss of performance. The results collected in this study have the potential to greatly benefit the design of OFMs with better friction performance. Moreover, the computational approach we proposed could save a dramatic amount of time and expenses that are currently injected into the organic friction modifiers research and development.

4. Materials and methods

4.1. Materials

Commercial lubricant products are complex mixtures of additives, including friction modifiers, embedded in a base lubricant oil. In our study, squalane was used as the base oil. Squalane is the hydrogenated derivative of squalene and it is used as a common reference model for base oil in tribology applications [46]. We considered five Organic friction Modifiers (OFM): Oleic Acid — OA, Oleic Amide — OAm, Glycerol Monooleate — GMO (all purchased from Sigma Aldrich), XTJ785 (Petronas lubricants), PC21 (developed at the DOWNSTREAM lab at Eni S.p.A). The chemical structure of the base oil and the OFMs are provided in Fig. 9.

4.2. Experimental methods

4.2.1. Friction coefficient measurements

To characterize the tribological properties of the material at conditions representative of the ones of a lubricant oil inside a motor engine [47], we have followed the following procedure to produce a tribofilm for spectroscopic analysis: An AISI52100 steel mini-traction machine (MTM) sample is sent for tribological measurement on a PCS instruments MTM tribometer. The instrument mounts a chamber in which the lubricant mix is contained. A ball of the same material as the MTM sample is immersed in the lubricant mix and fixed on a rotating axis. The lubricant mix is composed of 99% wt. of squalane and 1% wt. of the selected OFM. The ball is then put in contact with the sample and the instrument is turned on and the measurement starts. The friction coefficient is measured as a function of entrainment speed, while keeping the load, the sliding/rolling ratio, and the temperature constant instead. In our experiments, the curves were obtained maintaining a constant normal load of 30 N and 50% sliding/rolling ratio. The friction curves are measured starting from high values of entrainment speed (2 m/s in our case) up to very low ones (0.004 m/s). A representative example of a friction coefficient curve recorded by the PCS tribometer is reported in Section SI.7 of the Supporting Information. The variance in the data points was investigated previously in the Eni laboratories and was ascribed to the fact that when the lubricant mixture is made by squalane (base oil) and the friction modifier only, the viscosity of the base oil plays an important role in the friction performances at the very start of the tribological measurement, increasing the variance of the tribological results (is also to avoid this phenomenon that viscosity modifiers are added in the commercial lubricant mix).

4.2.2. Micro-IRRAS spectra

A Bruker Hyperion Spectrometer mounting a micro-GIR (Grazing Incidence IR) objective was used to perform micro-IRRAS measurements. The micro-GIR objective uses a set of mirror lenses to obtain a grazing-angle reflection on a microscopic scale. For each OFM, the micro-IRRAS spectra were recorded on the sample produced by the MTM measurements, both inside and outside the wear track. The maximum size of the area probed by the micro-IRRAS measurement is $\approx$160 μm × 160 μm, which is well inside the width of the wear track etched on the MTM sample during the tribological measurements ($\approx$200 μm in width). The spectra were recorded with 2048 scans and a resolution of 8 cm^{-1}.

4.3. Theoretical methods

4.3.1. Computational model systems

Hematite: As a model system for the iron surface, we selected the Fe-O3-Fe-R (0001) hematite surface (See supplementary information, Section SI-1) [48]. This single-Fe terminated surface is shown to be the most thermodynamically stable at room temperature by theoretical and experimental studies [48,49] and it has been reported in the literature to be the most common product of steel corrosion [50]. The structure
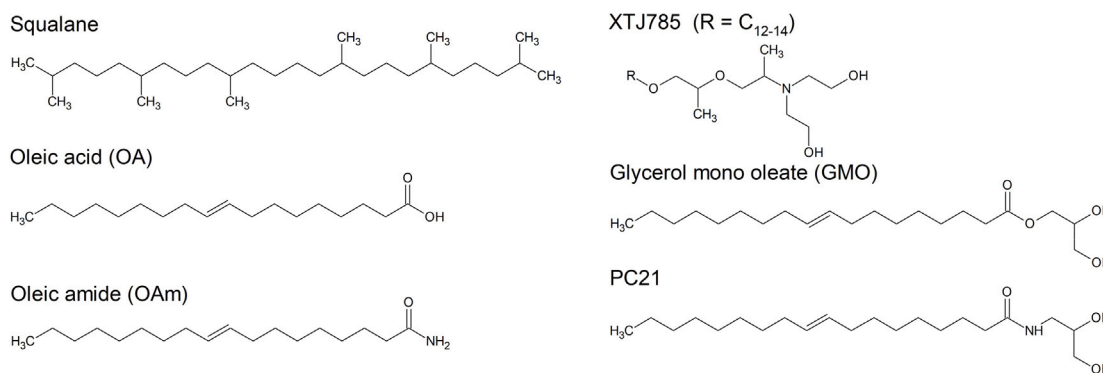
Fig. 9. Chemical structures of the base reference oil squalane and the OFM molecules investigated in this study.

of the Fe_2O_3 (0001) plane is composed of alternated layers of oxygen atoms and bilayers of iron atoms. Overall the slab is antiferromagnetic, as the whole structure is a stack of alternated spin-up and spin-down ferromagnetic layers.

OFMs: The alkyl chains of the OFM molecules have been modeled by six carbon atoms, instead of the complete eighteen carbons of the real molecules. This is a fair compromise between accuracy and computational cost as it has been shown in the past that the structure and electronic properties of the head groups of the kind of SAMs discussed in this paper are not strongly affected by the alkyl chain length [51].

We will refer to these model structures as OA_{C6}, OAm_{C6}, GMO_{C6}, $XTJ785_{C6}$, and $PC21_{C6}$.

4.3.2. Static DFT

The structure, vibrational spectra, and energetics (electronic energy and free energy) of Self Assembly Monolayer(SAM) of OA_{C6}, OAm_{C6}, GMO_{C6}, $XTJ785_{C6}$, and $PC21_{C6}$ adsorbed on iron have been characterized by static periodic DFT calculations using the code CRYSTAL17 [52] in a high coverage regime: one molecule per unit cell (see Tables S1 and S2 of the Supporting Information for more details). The procedure used is the same already described in Ref. [12]. We selected the B3LYP [53–55] functional together with a Gaussian-type POB-DZVP basis set as a reasonable compromise between accuracy and computational cost [56]. A correction for dispersion interactions was included in the calculations through Grimme's D3(BJ) correction [57–59]. Two-dimensional periodic boundary conditions (slab model) were applied along the surface. The antiferromagnetism of hematite has been included in the CRYSTAL17 calculation by controlling the alpha and beta spins population of the iron sites [60,61].

For all the systems discussed in this paper, we performed a full geometry relaxation of both the cell parameters and the atomic positions for the isolated hematite slab (hem), the isolated molecule (mol), the isolated SAM (SAM), and the SAM adsorbed at the hematite surface ($SAM@hem$). The adsorption energy is calculated as

$$\Delta E_{ads} = \frac{E_{SAM@hem} - (E_{hem} - N \cdot E_{mol})}{N} \quad (2)$$

where N is the number of molecules per unit cell (one in our case). We then calculated the packing energy of the SAM as

$$\Delta E_{pack} = \frac{E_{SAM} - N \cdot E_{mol}}{N} \quad (3)$$

and the contribution of the interaction between the OFM head and the hematite surface as

$$\Delta E_{adh} = \Delta E_{ads} - \Delta E_{pack} \quad (4)$$

The IR absorption spectra have been then computed on the optimized structure in the double harmonic approximation. The selection rules of IRRAS spectroscopy have been taken into account by projecting

the transition dipole moment on a unitary vector perpendicular to the hematite surface and considering only this component in the IR activity. Additionally, to have a qualitative idea of the effect of a tilt of OFMs on the IRRAS spectra, we also considered the IRRAS spectrum generated by the component of transition dipole moment projected on unitary vectors tilted with an angle 0, 5, 10, 15, 20, 25 and 30 degrees from the vertical position (see supplementary information — Section SI-3). Finally, we have computed the Gibbs free energy of adsorption (ΔG_{ads}) for the system, to characterize the energetics ruling the stability of the adsorbed film.

$$\Delta G_{ads} = \frac{G_{SAM@hem} - (G_{hem} - N \cdot G_{mol})}{N} \quad (5)$$

where N is again the number of molecules per unit cell (one in our case). Details on the calculation of each term can be found in the Supplementary Information — Section SI-6.

4.3.3. Classical MD simulations

The classical FF molecular dynamics of OA_{C6} were run with code LAMMPS (Large-scale Atomic/Molecular Massively Parallel Simulator) [62]. Following the strategy described in Ref. [63], for the hematite slab, we used a Buckingham potential with a Coulombic electrostatic term. Intermolecular interactions were instead described by a Lennard-Jones potential and a Coulombic electrostatic term. Finally, the L-OPLS-AA [64,65]. FF has been chosen for the OFMs and base lubricant oil. In Ref. [66], many non-reactive FFs have been benchmarked for the description of OFMs (or in general of long hydrocarbons), and it was found that L-OPLS-AA. [64,65] to be the one to be most consistent with the experimental values for a wide variety of macroscopic quantities. For the organic friction modifier, since the qualitative behavior of the friction coefficient at increasing temperature appears to be independent of the particular OFM (see Section 2.1), we have simulated OA_{C6} in its bidentate adsorption configuration on hematite. This is also due to the choice of the description of the OFM-hematite interaction, as the monodentate configuration would require the implementation of a reactive force field. This decision is not expected to impact the information gained by the simulations, for the aforementioned reasons. Moreover, we are mainly interested in the dynamics of the alkyl chain of the molecules, and the adsorption energies of the bidentate and monodentate configurations of OA_{C6} on hematite were found to be equivalent [12]. The initial geometry for the MD simulations was constructed using the VMD (Visual Molecular Dynamics) software [67]. The single-cell geometry from the CRYSTAL17 optimization was taken as the starting block, and a 10 × 10 slab was generated. A first set of simulations was run on the single 10 × 10 slab, to investigate the effect of temperature on the tribofilm without any external tribological force applied. The simulations were run at 300, 420, and 500 K, using a Nosé–Hoover thermostat (t_{thermo} = 40 fs) and barostat (t_{baro} = 400 fs) in the NVT ensemble.

After a first equilibration run of 1 ns, a production run of 2 ns was performed with a timestep of 0.5 fs. A copy of the 10 × 10 initial

slab was generated and placed on top of the first one mirroring it at a distance of 60 Å. This formed a space between the two slabs, which was filled with 75 molecules of squalane to simulate the base lubricant oil. The system was then subjected to a pressure of 0.5 GPa at 300, 420, and 500 K in separate simulations to squeeze the squalane between the two layers and form a sandwich-like structure. These structures were again equilibrated at the respective temperature for 0.5 ns.

The resulting systems were used as starting points for the simulation of the tribological phenomena (i.e., the two slabs sliding on each other in opposite directions). To simulate the action of an engine piston a velocity is applied to the outermost hematite layers of the two slabs in opposite directions of ± 0.5 m/s, for a total relative velocity of 1 m/s, which is in the range of velocities applied in the tribological MTM tests, corresponding to the boundary-mixed lubrication region. To investigate the effect of temperature, simulations were carried out at 300, 420, and 500 K. The pressure was kept at 0.5 GPa for the entire duration of the simulations. This set of simulations was run for a total of 2.5 ns, and the sliding direction was inverted two times: the first time at $t = 0.5$ ns, and then a second inversion at $t = 1.5$ ns.

Associated content

Input files associated with the MD, DFT, and DFT-MD simulations are available upon request.

CRediT authorship contribution statement

Nicolò S. Villa: Writing – review & editing, Writing – original draft, Visualization, Investigation, Formal analysis. **Lucia Bonoldi:** Writing – review & editing, Validation, Supervision, Resources, Conceptualization. **Giulio Assanelli:** Resources, Conceptualization, Validation. **Marcello Notari:** Conceptualization, Resources, Validation. **Andrea Lucotti:** Conceptualization, Supervision, Validation, Writing – review & editing. **Matteo Tommasini:** Writing – review & editing, Conceptualization, Supervision, Validation. **Herma M. Cuppen:** Writing – review & editing, Validation, Supervision, Methodology, Conceptualization. **Daria R. Galimberti:** Conceptualization, Methodology, Supervision, Validation, Writing – review & editing.

Declaration of competing interest

The authors declare that they have no known competing financial interests or personal relationships that could have appeared to influence the work reported in this paper.

Data availability

Data will be made available on request.

Acknowledgments

Appendix A. Supplementary data

Additional details on the Model Setup for the Hematite slab model and adsorbed SAM model. Additional details on the classical MD Simulations setup. Polarized calculated harmonic spectra. Computational details of DFT-MD simulations and discussion on the computed spectra with this technique. Computed Electronic and Free energies of adsorptions for all the analyzed systems.

Supplementary material related to this article can be found online at https://doi.org/10.1016/j.triboint.2024.109649.

References

[1] Holmberg K, Erdemir A. Influence of tribology on global energy consumption, costs and emissions. Friction 2017;5:263–84. http://dx.doi.org/10.1007/s40544-017-0183-5.

[2] Spikes H. Friction modifier additives. Tribol Lett 2015;60:5. http://dx.doi.org/10.1007/s11249-015-0589-z.

[3] Allen C, Drauglis E. Boundary layer lubrication: monolayer or multilayer. Wear 1969;14(5):363–84. http://dx.doi.org/10.1016/0043-1648(69)90017-9, URL https://www.sciencedirect.com/science/article/pii/0043164869900179.

[4] Loehlé S, Matta C, Minfray C, Mogne T, Iovine R, Obara Y, Miyamoto A, Martin JM. Mixed lubrication of steel by C18 fatty acids revisited. Part I: Toward the formation of carboxylate. Tribol Int 2015;82:218–27. http://dx.doi.org/10.1016/j.triboint.2014.10.020, URL https://www.sciencedirect.com/science/article/pii/S0301679X14003776.

[5] Anghel V, Cann PM, Spikes HA. Direct measurement of boundary lubricating films. Tribology series, vol. 32, Elsevier; 1997, p. 459–66. http://dx.doi.org/10.1016/S0167-8922(08)70473-5, URL https://www.sciencedirect.com/science/article/pii/S0167892208704735.

[6] Fry BM, Moody G, Spikes HA, Wong JSS. Adsorption of organic friction modifier additives. Langmuir 2020;36(5):1147–55. http://dx.doi.org/10.1021/acs.langmuir.9b03668.

[7] Casford MTL, Davies PB. The structure of oleamide films at the aluminum/oil interface and aluminum/air interface studied by sum frequency generation (SFG) vibrational spectroscopy and reflection absorption infrared spectroscopy (RAIRS). ACS Appl Mater Interfaces 2009;1(8):1672–81. http://dx.doi.org/10.1021/am900199f.

[8] Simič R, Kalin M. Adsorption mechanisms for fatty acids on DLC and steel studied by AFM and tribological experiments. Appl Surf Sci 2013;283:460–70. http://dx.doi.org/10.1016/j.apsusc.2013.06.131, URL https://www.sciencedirect.com/science/article/pii/S0169433213012440.

[9] Lim MS, Feng K, Chen X, Wu N, Raman A, Nightingale J, Gawalt ES, Korakakis D, Hornak LA, Timperman AT. Adsorption and desorption of stearic acid self-assembled monolayers on aluminum oxide. Langmuir 2007;23(5):2444–52. http://dx.doi.org/10.1021/la061914n.

[10] Bowden F, Gregory J, Tabor D. Lubrication of metal surfaces by fatty acids. Nature 1945;156(3952):97–101.

[11] Wood MH, Casford M, Steitz R, Zarbakhsh A, Welbourn RJL, Clarke SM. Comparative adsorption of saturated and unsaturated fatty acids at the iron oxide/oil interface. Langmuir 2016;32(2):534–40. http://dx.doi.org/10.1021/acs.langmuir.5b04435.

[12] Villa N, Serra G, Bonoldi L, Assanelli G, Notari M, Lucotti A, Tommasini M. Combining micro-infrared reflection absorption spectroscopy with density functional theory for investigating the adsorption of organic friction modifiers on steel surfaces. Vib Spectrosc 2022;121:103403. http://dx.doi.org/10.1016/j.vibspec.2022.103403, URL https://www.sciencedirect.com/science/article/pii/S0924203122000704.

[13] Hou J, Tsukamoto M, Zhang H, Fukuzawa K, Itoh S, Azuma N. Characterization of organic friction modifiers using lateral force microscopy and eyring activation energy model. Tribol Int 2023;178:108052. http://dx.doi.org/10.1016/j.triboint.2022.108052.

[14] Cyriac F, Tee X, Poornachary SK, Chow P. Influence of structural factors on the tribological performance of organic friction modifiers. Friction 2021;9:380–400. http://dx.doi.org/10.1007/s40544-020-0385-0.

[15] Jahanmir S, Beltzer M. Effect of additive molecular structure on friction coefficient and adsorption. J Tribol 1986;108(1):109–16. http://dx.doi.org/10.1115/1.3261129.

[16] Frewing JJ, Taylor GI. The influence of temperature on boundary lubrication. Proc R Soc Lond Ser A 1942;181(984):23–42. http://dx.doi.org/10.1098/rspa.1942.0056.

[17] Gattinoni C, Ewen JP, Dini D. Adsorption of surfactants on α-Fe_2O_3(0001): A density functional theory study. J Phys Chem C 2018;122(36):20817–26. http://dx.doi.org/10.1021/acs.jpcc.8b05899.

[18] Jaishankar A, Jusufi A, Vreeland JL, Deighton S, Pellettiere J, Schilowitz AM. Adsorption of stearic acid at the iron oxide/oil interface: theory, experiments, and modeling. Langmuir 2019;35(6):2033–46. http://dx.doi.org/10.1021/acs.langmuir.8b03132.

[19] Doig M, Warrens CP, Camp PJ. Structure and friction of stearic acid and oleic acid films adsorbed on iron oxide surfaces in squalane. Langmuir 2014;30(1):186–95. http://dx.doi.org/10.1021/la404024v.

[20] Zheng X, Zhu H, Kosasih B, Tieu AK. A molecular dynamics simulation of boundary lubrication: The effect of n-alkanes chain length and normal load. Wear 2013;301(1–2):62–9. http://dx.doi.org/10.1016/j.wear.2013.01.052.

[21] Bradley-Shaw JL, Camp PJ, Dowding PJ, Lewtas K. Molecular dynamics simulations of glycerol monooleate confined between mica surfaces. Langmuir 2016;32(31):7707–18. http://dx.doi.org/10.1021/acs.langmuir.6b00091.

[22] Loehle S, Matta C, Minfray C, Le-Mogne T, Iovine R, Obara Y, Miyamoto A, Martin J. Mixed lubrication of steel by C18 fatty acids revisited part II: Influence of some key parameters. Tribol Int 2015;94. http://dx.doi.org/10.1016/j.triboint.2015.08.036.

[23] Chen X, Yang J, Yasuda K, Koga N, Zhang H. Adsorption behavior of TEMPO-based organic friction modifiers during sliding between iron oxide surfaces: A molecular dynamics study. Langmuir 2022;38(10):3170–9. http://dx.doi.org/10.1021/acs.langmuir.1c03203.

[24] Acero PN, Mohr S, Bernabei M, Fernández C, Domínguez B, Ewen JP. Molecular simulations of surfactant adsorption on iron oxide from hydrocarbon solvents. Langmuir 2021;37(50):14582–96. http://dx.doi.org/10.1021/acs.langmuir.1c02133.

[25] Pominov A, Müller-Hillebrand J, Träg J, Zahn D. Interaction models and molecular simulation systems of steel–organic friction modifier interfaces. Tribol Lett 2021;69:1–8. http://dx.doi.org/10.1007/s11249-020-01384-9.

[26] Ouyang C, Bai P, Wen X, Zhang X, Meng Y, Ma L, Tian Y. Effects of conformational entropy on antiwear performances of organic friction modifiers. Tribol Int 2021;156:106848. http://dx.doi.org/10.1016/j.triboint.2020.106848.

[27] Ewen JP, Gattinoni C, Morgan N, Spikes HA, Dini D. Nonequilibrium molecular dynamics simulations of organic friction modifiers adsorbed on iron oxide surfaces. Langmuir 2016;32(18):4450–63. http://dx.doi.org/10.1021/acs.langmuir.6b00586.

[28] Ewen JP, Restrepo SE, Morgan N, Dini D. Nonequilibrium molecular dynamics simulations of stearic acid adsorbed on iron surfaces with nanoscale roughness. Tribol Int 2017;107:264–73. http://dx.doi.org/10.1016/j.triboint.2016.11.039.

[29] Lu X, Khonsari MM, Gelinck ERM. The stribeck curve: Experimental results and theoretical prediction. J Tribol 2006;128(4):789–94.

[30] Spikes HA. Mixed lubrication – an overview. Lubr Sci 1997;9(3):221–53. http://dx.doi.org/10.1002/ls.3010090302, URL https://onlinelibrary.wiley.com/doi/abs/10.1002/ls.3010090302.

[31] Zhu D. Elastohydrodynamic lubrication (EHL). In: Wang QJ, Chung Y, editors. Encyclopedia of tribology. Springer US; 2013, p. 874–89. http://dx.doi.org/10.1007/978-0-387-92897-5_624.

[32] Minami I. Molecular science of lubricant additives. Appl Sci 2017;7(5). http://dx.doi.org/10.3390/app7050445, URL https://www.mdpi.com/2076-3417/7/5/445.

[33] Lattuada MMF, Manni M. The roadmap towards CO 2 reduction: evaluation of new proprietary organic friction reducer additives. Technical report, SAE Technical Paper; 2022.

[34] Spikes HA. Film-forming additives - direct and indirect ways to reduce friction. Lubr Sci 2002;14(2):147–67. http://dx.doi.org/10.1002/ls.3010140204, URL https://onlinelibrary.wiley.com/doi/abs/10.1002/ls.3010140204.

[35] Chandross M, Webb EB, Stevens MJ, Grest GS, Garofalini SH. Systematic study of the effect of disorder on nanotribology of self-assembled monolayers. Phys Rev Lett 2004;93:166103. http://dx.doi.org/10.1103/PhysRevLett.93.166103.

[36] Kong Y, Tildesley D, Alejandre J. The molecular dynamics simulation of boundary-layer lubrication. Mol Phys 1997;92(1):7–18. http://dx.doi.org/10.1080/002689797170554.

[37] Ruths M, Lundgren S, Danerlöv K, Persson K. Friction of fatty acids in nanometer-sized contacts of different adhesive strength. Langmuir 2008;24(4):1509–16. http://dx.doi.org/10.1021/la7023633.

[38] Lee D, Oh T, Cho K. Combined effect of chain length and phase state on adhesion/friction behavior of self-assembled monolayers. J Phys Chem B 2005;109(22):11301–6. http://dx.doi.org/10.1021/jp051232t.

[39] Campen S, Green J, Lamb G, Atkinson D, Spikes H. On the increase in boundary friction with sliding speed. Tribol Lett 2012;48:237–48. http://dx.doi.org/10.1007/s11249-012-0019-4.

[40] He G, Robbins MO. Simulations of the kinetic friction due to adsorbed surface layers. Tribol Lett 2001;10(1–2):7–14. http://dx.doi.org/10.1023/A:1009030413641.

[41] Wood MH, Welbourn RJ, Charlton T, Zarbakhsh A, Casford M, Clarke SM. Hexadecylamine adsorption at the iron oxide–oil interface. Langmuir 2013;29(45):13735–42.

[42] Ramin L, Jabbarzadeh A. Frictional properties of two alkanethiol self assembled monolayers in sliding contact: Odd-even effects. J Chem Phys 2012;137(17). http://dx.doi.org/10.1063/1.4764301.

[43] Mikulski PT, Gao G, Chateauneuf GM, Harrison JA. Contact forces at the sliding interface: Mixed versus pure model alkane monolayers. J Chem Phys 2005;122(2). http://dx.doi.org/10.1063/1.1828035.

[44] Fry BM, Moody G, Spikes H, Wong J. Effect of surface cleaning on performance of organic friction modifiers. Tribol Trans 2020;63(2):305–13. http://dx.doi.org/10.1080/10402004.2019.1687797.

[45] Blanck S, Martí C, Loehlé S, Steinmann SN, Michel C. (Dis) similarities of adsorption of diverse functional groups over alumina and hematite depending on the surface state. J Chem Phys 2021;154(8). http://dx.doi.org/10.1063/5.0038412.

[46] Apòstolo RFG, Tsagkaropoulou G, Camp PJ. Molecular adsorption, self-assembly, and friction in lubricants. J Mol Liq 2019;277:606–12. http://dx.doi.org/10.1016/j.molliq.2018.12.099, URL https://www.sciencedirect.com/science/article/pii/S0167732218356502.

[47] Lattuada M, Manni M. A new methodology for the experimental evaluation of organic antifriction additives. In: Proceedings of the ISFL, international symposium on fuel and lubricants, new Delhi, India. 2016, p. 18–20.

[48] Schöttner L, Ovcharenko R, Nefedov A, Voloshina E, Wang Y, Sauer J, Wöll C. Interaction of water molecules with the α-Fe$_2$O$_3$(0001) surface: A combined experimental and computational study. J Phys Chem C 2019;123(13):8324–35. http://dx.doi.org/10.1021/acs.jpcc.8b08819.

[49] Parkinson GS. Iron oxide surfaces. Surf Sci Rep 2016;71(1):272–365. http://dx.doi.org/10.1016/j.surfrep.2016.02.001, URL https://www.sciencedirect.com/science/article/pii/S0167572916000054.

[50] Dwivedi D, Lepková K, Becker T. Carbon steel corrosion: a review of key surface properties and characterization methods. RSC Adv 2017;7:4580–610. http://dx.doi.org/10.1039/C6RA25094G.

[51] Rayne S, Forest K. Theoretical studies on the pka values of perfluoroalkyl carboxylic acids. J Mol Struct: THEOCHEM 2010;949(1):60–9. http://dx.doi.org/10.1016/j.theochem.2010.03.003, URL https://www.sciencedirect.com/science/article/pii/S0166128010001867.

[52] Dovesi R, Erba A, Orlando R, Zicovich-Wilson CM, Civalleri B, Maschio L, Rérat M, Casassa S, Baima J, Salustro S, Kirtman B. Quantum-mechanical condensed matter simulations with CRYSTAL. WIREs Comput Mol Sci 2018;8(4):e1360. http://dx.doi.org/10.1002/wcms.1360, URL https://wires.onlinelibrary.wiley.com/doi/abs/10.1002/wcms.1360.

[53] Becke AD. Density-functional exchange-energy approximation with correct asymptotic behavior. Phys Rev A 1988;38:3098–100. http://dx.doi.org/10.1103/PhysRevA.38.3098, URL https://link.aps.org/doi/10.1103/PhysRevA.38.3098.

[54] Lee C, Yang W, Parr RG. Development of the colle-salvetti correlation-energy formula into a functional of the electron density. Phys Rev B 1988;37:785–9. http://dx.doi.org/10.1103/PhysRevB.37.785, URL https://link.aps.org/doi/10.1103/PhysRevB.37.785.

[55] Vosko SH, Wilk L, Nusair M. Accurate spin-dependent electron liquid correlation energies for local spin density calculations: a critical analysis. Can J Phys 1980;58(8):1200–11. http://dx.doi.org/10.1139/p80-159.

[56] Vilela Oliveira D, Laun J, Peintinger MF, Bredow T. BSSE-correction scheme for consistent gaussian basis sets of double- and triple-zeta valence with polarization quality for solid-state calculations. J Comput Chem 2019;40(27):2364–76. http://dx.doi.org/10.1002/jcc.26013, URL https://onlinelibrary.wiley.com/doi/abs/10.1002/jcc.26013.

[57] Grimme S, Antony J, Ehrlich S, Krieg H. A consistent and accurate ab initio parametrization of density functional dispersion correction (DFT-D) for the 94 elements H-Pu. J Chem Phys 2010;132(15):154104. http://dx.doi.org/10.1063/1.3382344.

[58] Grimme S, Ehrlich S, Goerigk L. Effect of the damping function in dispersion corrected density functional theory. J Comput Chem 2011;32(7):1456–65. http://dx.doi.org/10.1002/jcc.21759, URL https://onlinelibrary.wiley.com/doi/abs/10.1002/jcc.21759.

[59] Grimme S, Hansen A, Brandenburg JG, Bannwarth C. Dispersion-corrected mean-field electronic structure methods. Chem Rev 2016;116(9):5105–54. http://dx.doi.org/10.1021/acs.chemrev.5b00533.

[60] Martin GJ, Cutting RS, Vaughan DJ, Warren MC. Bulk and key surface structures of hematite, magnetite, and goethite: A density functional theory study. Am Mineral 2009;94(10):1341–50. http://dx.doi.org/10.2138/am.2009.3029.

[61] Ferrero M, Rérat M, Kirtman B, Dovesi R. Calculation of first and second static hyperpolarizabilities of one- to three-dimensional periodic compounds. Implementation in the CRYSTAL code.. J Chem Phys 2008;129(24):244110. http://dx.doi.org/10.1063/1.3043366.

[62] Thompson AP, Aktulga HM, Berger R, Bolintineanu DS, Brown WM, Crozier PS, in 't Veld PJ, Kohlmeyer A, Moore SG, Nguyen TD, Shan R, Stevens MJ, Tranchida J, Trott C, Plimpton SJ. LAMMPS - a flexible simulation tool for particle-based materials modeling at the atomic, meso, and continuum scales. Comput Phys Comm 2022;271:108171. http://dx.doi.org/10.1016/j.cpc.2021.108171.

[63] Tadmor EB, Elliott RS, Sethna JP, Miller RE, Becker CA. The potential of atomistic simulations and the knowledgebase of interatomic models. JOM 2011;63(7):17. http://dx.doi.org/10.1007/s11837-011-0102-6.

[64] Siu SWI, Pluhackova K, Böckmann RA. Optimization of the OPLS-AA force field for long hydrocarbons. J Chem Theory Comput 2012;8(4):1459–70. http://dx.doi.org/10.1021/ct200908r.

[65] Jorgensen WL, Maxwell DS, Tirado-Rives J. Development and testing of the OPLS all-atom force field on conformational energetics and properties of organic liquids. J Am Chem Soc 1996;118(45):11225–36. http://dx.doi.org/10.1021/ja9621760.

[66] Ewen JP, Gattinoni C, Thakkar FM, Morgan N, Spikes HA, Dini D. A comparison of classical force-fields for molecular dynamics simulations of lubricants. Materials 2016;9(8). http://dx.doi.org/10.3390/ma9080651, URL https://www.mdpi.com/1996-1944/9/8/651.

[67] Humphrey W, Dalke A, Schulten K. VMD - visual molecular dynamics. J Mol Graph 1996;14:33–8. http://dx.doi.org/10.1016/0263-7855(96)00018-5.